Valley polarization and photocurrent generation in transition metal dichalcogenide alloy $MoS_{2x}Se_{2(1-x)}$

Chumki Nayak,[1] Suvadip Masanta,[1] Sukanya Ghosh,[2,*] Shubhadip Moulick,[3] Atindra Nath Pal,[3] Indrani Bose,[1] and Achintya Singha[1,†]

[1]*Department of Physical Sciences, Bose Institute, 93/1, Acharya Prafulla Chandra Road, Kolkata 700009, India*

[2]*Department of Physics and Astronomy, Uppsala University, Box-516, 75120 Uppsala, Sweden*

[3]*Department of Condensed Matter and Materials Physics, S. N. Bose National Centre for Basic Sciences, Kolkata 700106, India*

(Received 14 December 2023; revised 22 February 2024; accepted 23 February 2024; published 20 March 2024)

Monolayer transition metal dichalcogenides (TMDCs) constitute the core group of materials in the emerging semiconductor technology of valleytronics. While the coupled spin-valley physics of pristine TMDC materials and their heterostructures has been extensively investigated, less attention has been given to TMDC alloys, which could be useful in optoelectronic applications due to the tunability of their band gaps. The experimental investigations presented herein focus on the exploration of the spin-valley physics of the monolayer and bilayer TMDC alloy $MoS_{2x}Se_{2(1-x)}$ in terms of valley polarization and the generation as well as electrical control of a photocurrent utilizing the circular photogalvanic effect. Piezoelectric force microscopy provides evidence for an internal electric field perpendicular to the alloy layer, thus breaking the out-of-plane mirror symmetry. The experimental observation is supported by first-principles calculations based on the density functional theory. A comparison of the photocurrent device, based on the alloy material, is made with similar devices involving other TMDC materials.

DOI: 10.1103/PhysRevB.109.115304

I. INTRODUCTION

The two-dimensional (2D) transition metal dichalcogenides (TMDCs) with the chemical formula MX_2, where $M =$ Mo, W and $X =$ S, Se, Te are a transition metal and a chalcogen atom, respectively, have drawn significant attention from researchers in recent years. This is because of their immense application potential in semiconductor-based technologies like valleytronics, which exploits the valley degree of freedom besides those of spin and charge [1–4]. The combination of time-reversal symmetry, broken inversion symmetry, and the presence of significant spin-orbit interactions involving the "heavy" d electrons of the transition metal ions gives rise to spin-valley locking and valley-specific physical properties and phenomena. Figures 1(a) and 1(b) show the coexistence of a pair of valence band (VB) and conduction band (CB) valleys in the band structure located at two inequivalent points K and K' in momentum space with the K and K' valleys related to each other via time-reversal symmetry. The Zeeman-type splitting of the spin-degenerate VB and CB, a consequence of broken in-plane inversion symmetry and spin-orbit interactions, is shown with the split subbands designated as VB−, VB+, CB−, and CB+ in order of increasing energy. The splitting in the case of the VB is an order of magnitude larger than that of the CB. The split VB subbands are spin polarized, with the electron spins oriented in the out-of-plane direction (up or down). Due to time-reversal symmetry, the polarizations of the subbands are reversed at the K and K' valleys. This gives rise to the unique feature of spin-valley locking in the monolayer implying that the spin and valley degrees of freedom are coupled [1,2,5].

Focusing on the TMDC monolayer material MoX_2, there are two other distinct classes of related monolayer materials: the Janus TMDC materials, $MoXY$ (X, $Y =$ S, Se; $X \neq Y$) and the TMDC alloy (TMDCA) $MoS_{2x}Se_{2(1-x)}$ ($0 \leqslant x \leqslant 1$). The three classes of monolayer materials have a common structural ingredient, namely, a central layer of Mo atoms. This layer is sandwiched between two layers of chalcogen atoms. In the monolayer Janus MoSSe, one chalcogen layer is occupied by S atoms and the other layer by Se atoms, thus breaking the out-of-plane mirror symmetry. The polar nature of the material generates an electric dipole moment with its associated electric field perpendicular to the monolayer. This intrinsic electric field generates the Rashba spin-orbit interactions which split the VB at the Γ point in momentum space. In the monolayer TMDCA, the chalcogen layers are randomly decorated with the S and Se atoms [Fig. 1(c)] introducing disorder in the system. In this context, two pertinent questions are whether the universal features of the spin-valley physics of pristine TMDC materials survive in the presence of disorder and whether an intrinsically generated out-of-plane electric field is present in the alloy, as in the case of the Janus material, or disorder averages the field to be zero. From an application point of view, the issues are tied to the possibility of constructing photocurrent devices based on monolayer and bilayer TMDCA materials.

*Present address: Department of Physics, Bangabasi Morning College, 19 Rajkumar Chakraborty Sarani, Kolkata 700009, India.

†achintya@jcbose.ac.in

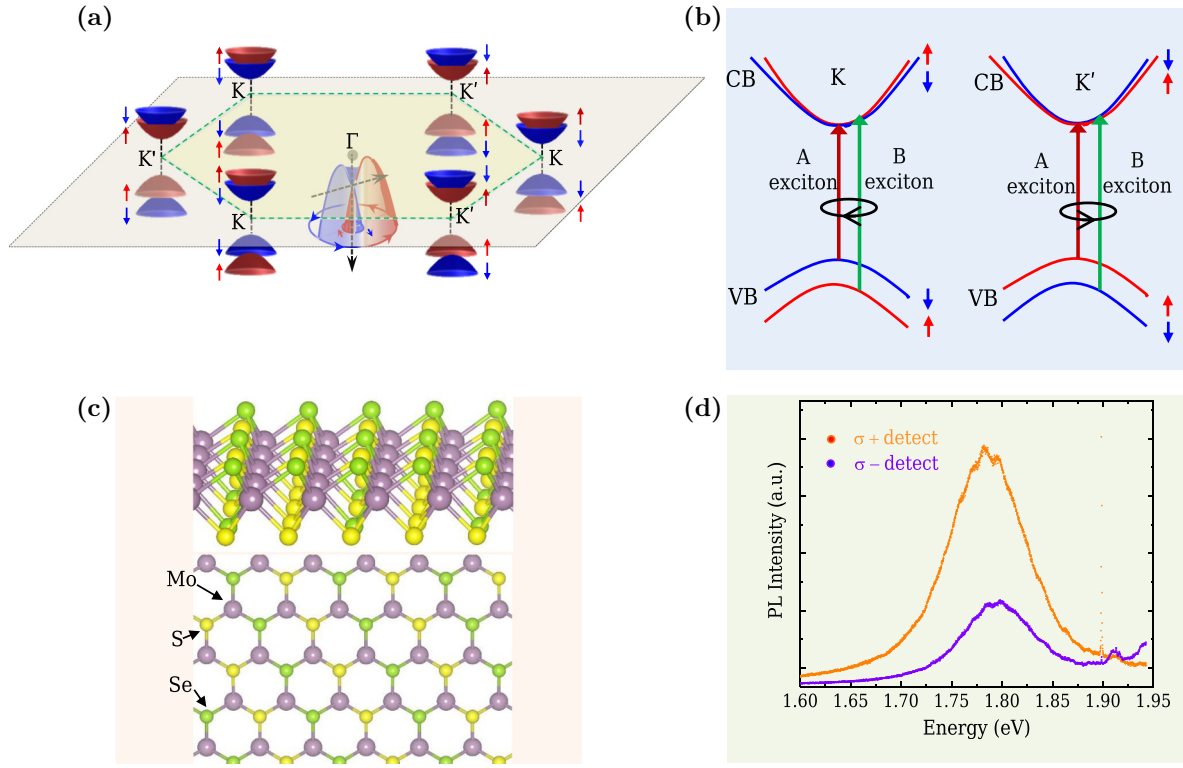

FIG. 1. Schematic representation of Brillouin zone, band diagram of K, K' valleys, crystal structure, and PL of monolayer TMDCA. (a) Schematic representation of the valley structures at the K, K', and Γ points of Brillouin zone. (b) Interband transitions at K and K' points under right and left circularly polarized light resulting in the formations of A and B excitons. (c) Side (upper panel) and top (lower panel) views of monolayer TMDCA structure. (d) Polarization-dependent PL measurement under near-on-resonance laser excitation energy (1.96 eV).

In the cases of multilayer and bulk TMDC materials, the band gap is indirect and the inversion symmetry is not broken when the number of layers is even. The breaking of the inversion symmetry in bilayer TMDC materials, an essential requirement for applications involving valley-contrasting properties, is achieved by applying an external electric field perpendicular to the bilayer [6], resulting in a potential difference between the layers. In this context, the Janus TMDC materials are of special note as the inversion symmetry is intrinsically broken for both the odd and even multilayer materials thus bypassing the necessity of using an external electric field [7,8]. In our study, we investigated the spin-valley physics of the monolayer and bilayer TMDCA through experiments as well as first-principles calculations based on density functional theory (DFT). We carried out polarization-resolved photoluminescence (PL) and photocurrent generation experiments using off- and near-on-resonance lasers with energies of 2.54 eV and 1.96 eV, respectively. In the case of the off-resonance laser excitation, the experimental measurements of the degrees of valley and photocurrent polarization of monolayer TMDCA yielded some surprising features. The optical and electrical control of the photocurrent was brought about by changing the polarization of the laser light and applying an external electric field via a gate voltage. The results obtained clearly establish the conceptual validity of the spin-valley physics in the presence of disorder in the chalcogen layers of the alloy material. The result is not surprising as the predominant contributions to the valley physics come from the d electrons of the Mo atoms located in the central layer, which is the common feature in all three classes of TMDC materials. The disorder in the chalcogen layers could in principle yield a zero-average out-of-plane electric dipole moment and field. To check this, piezoelectric force microscopy (PFM) was used which provides clear evidence for the existence of a finite internal electric field perpendicular to the TMDCA monolayer. The photocurrent device based on the monolayer/bilayer alloy material was shown to compare quite well, performance-wise, and in certain respects better, with similar devices involving other TMDC materials. Our study provides experimental demonstration of the generation of a photocurrent in monolayer and bilayer TMDCA samples. Earlier experimental studies [9–13] were focused on monolayer/bilayer/bulk TMDC materials with no study reported so far on the Janus material MoSSe or the related class of TMDCA materials.

II. METHODS

Sample growth

TMDCA monolayer and bilayer samples were synthesized on a SiO_2 (thickness: 300 nm)/doped Si substrate using the chemical vapor deposition (CVD) method in a homemade horizontal tube furnace connected to a vacuum pump. A schematic representation of the CVD setup and reagents used for the synthesis are given in Supplemental Note 2 of the Supplemental Material [14]. During the synthesis process, we optimized various parameters, including the distances between the Mo, S, and Se sources, temperature, and flow rates.

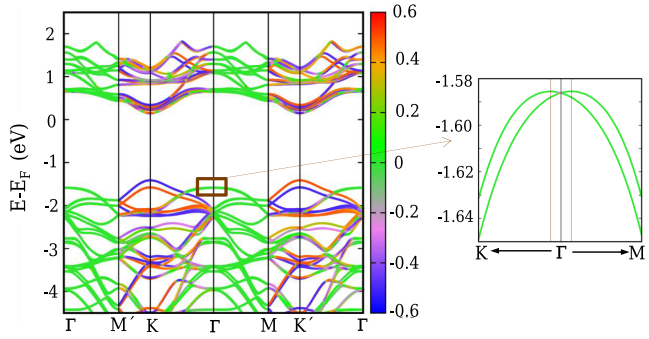

FIG. 2. DFT-calculated electronic band structure of monolayer TMDCA. It shows the electronic band structure for MoSSe alloy projected on $\langle s_z \rangle$. The inset shows the magnified Rashba splitting close to the Γ point.

A quartz boat containing MoO_3 powder was placed within the tube in a high-temperature zone (∼750 °C), while the S and Se powders were positioned in a relatively low-temperature zone (∼200 °C). The temperature of the furnace was gradually increased at a rate of 25 °C/min with a flow 10 sccm of high-purity Ar gas, reaching its maximum temperature over a span of 30 minutes. The furnace was maintained at the maximum temperature for 10 minutes with 40 sccm Ar flow before being allowed to cool down naturally to room temperature. The details of the characterization tools, device fabrication method, and optoelectronic measurement setup are provided in Supplemental Note 2 [14].

III. RESULTS

A. First-principles calculations

The $k \cdot p$ model derivations and first-principles calculations are summarized in Supplemental Note 1 [14]. Figure 2 shows the fully relativistic band structure of the TMDCA alloy ($x = 0.6$) including spin-orbit coupling, along the high-symmetry directions in the Brillouin zone. The highest VB and the lowest CB spin splittings at the K, K' valleys have magnitudes ∼170 meV (Fig. 2) and ∼10 meV (Fig. S1 of the Supplemental Material [14]), respectively. The band structure for the alloy material is color-coded for the spin polarization component $\langle s_z \rangle$. The expectation values of the spin components corresponding to the ith-energy spinor eigenfunction, $\Psi_{i,\mathbf{k}}(\mathbf{r})$, are obtained as

$$\langle s_\alpha \rangle = \frac{1}{2} \frac{\langle \Psi_{i,k} | \sigma_\alpha | \Psi_{i,k} \rangle}{\langle \Psi_{i,k} | \Psi_{i,k} \rangle}, \tag{1}$$

where σ_α, $\alpha = x, y, z$, are the Pauli spin matrices. The band structure confirms the universal features of the spin-valley physics that the alloy material shares with Janus and TMDC monolayers [24–27], and as schematized in Figs. 1(a) and 1(b). In particular, the K and K' valleys exhibit opposite polarization values, $\langle s_z \rangle = \pm 1/2$, with the computed sequence of values for the split VB and CB bands as shown in Fig. 1(b). We carried out a PFM experiment to establish the presence of an intrinsic electric field E_{int} perpendicular to the TMDCA monolayer. The field is associated with the breaking of the out-of-plane mirror symmetry. The Rashba spin-orbit interaction is generated by E_{int}. The splitting of the VB at the Γ point (inset of Fig. 2) and in-plane spin texture (Fig. S4a [14]) observed in the first-principles calculations are consistent with the experimental result of a nonzero E_{int}. No Rashba splitting is seen in the pristine MoX_2 systems as the electric field $E_{\text{int}} = 0$ in these systems (see Fig. S5 [14]).

B. Experimental results

1. Sample characterizations

As-grown samples are checked using optical microscope. Triangular-shaped flakes of TMDCA are randomly distributed on the substrate, as shown in Fig. S7b [14]. A scanning electron microscopy (SEM) image of a single TMDCA flake is shown in Fig. S7c [14]. To determine the atomic percentage of Mo, S, and Se in the TMDCA, energy-dispersive x-ray spectroscopy (EDX) was performed. The EDX spectrum and estimated percentages of Mo, S, and Se from this study are given in Fig. S7d [14]. The atomic force microscopy (AFM) image and height profile of the TMDCA sample (see Fig. S8a [14]) indicate that its thickness is in the monolayer regime. The PL spectrum (Fig. S8b [14]) exhibits the components resulting from the recombination of the A and B excitons and also the A trion. The energy associated with the A trion, A exciton, and B exciton is determined to be 1.78 eV, 1.81 eV, and 1.95 eV, respectively. Figure S8c shows the Raman spectrum of the TMDCA sample, with the most prominent Raman modes observed being E_1^1, A_1^1, E_2^3, E_1^2, and A_1^2 at 231 cm^{-1}, 272 cm^{-1}, 368 cm^{-1}, 384 cm^{-1}, and 405 cm^{-1}, respectively [14]. These observed modes are consistent with previous reports [28–30]. The optical image of the phototransistor made of monolayer TMDCA using the technique mentioned in the device fabrication section (Supplemental Note 2 [14]) is presented in Fig. S8d [14]. The plot of photocurrent vs light excitation power density with source-drain bias, $V_{ds} = 1$ V, is depicted in Fig. S8e showing a linear dependence on illumination intensity [14]. All subsequent photocurrent measurements were conducted in this linear region. Figure S8f displays the transfer characteristics of the TMDCA phototransistor at $V_{ds} = 2$ V under both dark and illuminated conditions using an excitation wavelength of 488 nm [14]. The photocurrent shows a slight increase when the device is in the OFF state ($V_g < 10$) V. However, at $V_g > 10$ V, there is a rapid enhancement in the photocurrent. In this ON state, the current contribution arises not only from a significant increase in photogenerated carriers but also from carrier tunneling. All the subsequent measurements have been performed in the OFF state.

2. Piezoelectricity in TMDCA

To experimentally probe the existence of an out-of-plane dipole moment arising due to the out-of-plane asymmetry in the structure of our TMDCA samples, we performed PFM measurements on various samples with different thicknesses. The PFM is a powerful technique for assessing ferroelectric and piezoelectric phenomena at the nanoscale. Ferroelectrics exhibit spontaneous polarization due to the existence of permanent electric dipoles and constitute a subset of piezoelectric materials. The piezoresponse in PFM measurements utilizes

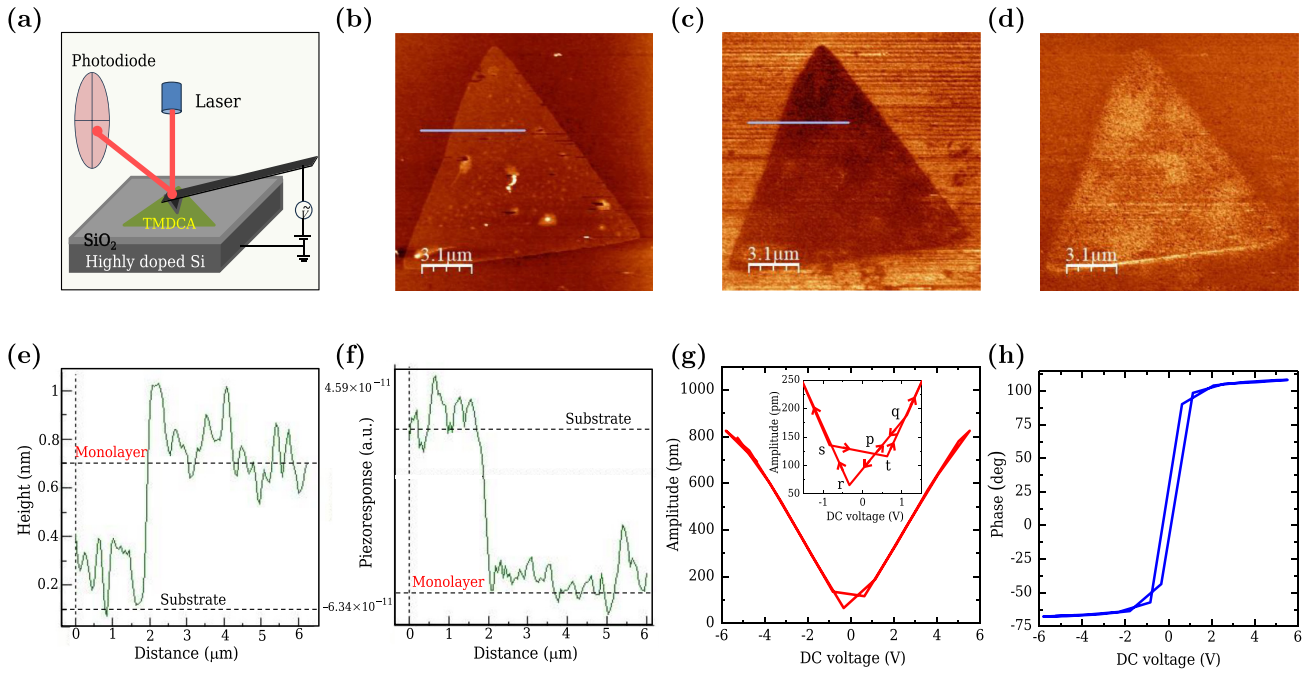

FIG. 3. PFM measurement on monolayer TMDCA. (a) Schematic representation of PFM measurement setup. (b) Topography, (c) piezoelectric amplitude, and (d) piezoelectric phase of triangular-shaped TMDCA on SiO_2/Si substrate. (e) Height and (f) piezoelectric amplitude line profiles corresponding to the cyan lines in images (b) and (c). (g) and (h) The PFM amplitude and phase of the TMDCA sample as a function of DC bias voltage.

the inverse piezo effect described as the development of mechanical strain in a piezoelectric material proportional to an applied voltage V with the proportionality constant known as the piezoelectric strain constant. A schematic representation of the experimental PFM setup is shown in Fig. 3(a). The voltage, applied to an AFM cantilever tip in contact with the sample, has both DC and AC components, $V_{\text{tip}} = V_{DC} + V_{AC}\cos(wt)$, where w is the frequency of the AC drive voltage. Since the focus of our PFM measurement is the detection of an out-of-plane electric dipole moment, the piezoresponse is measured in the vertical PFM mode in which the sample strain is measured in the z direction.

The sample material under the tip develops local surface deformations, either expansion or contraction, depending on whether the local sample polarization (associated with the vertical dipole moment) is parallel or antiparallel to the applied AC field. The periodic AC voltage generates an oscillatory movement of the sample surface which in turn is magnified by the periodic bending of the cantilever. The cantilever deflection is recorded as a change in the laser spot position on a photodetector. The local piezoelectric response of the sample surface is analyzed using a lock-in amplifier as the first harmonic component, A_{1w}, of the tip deflection, $A = A_0 + A_{1w}\cos(wt + \Phi)$, induced by the periodic AC voltage. The lock-in amplifier detection method allows for the minute surface deformations in the subnanometer range to be distinguished from the static topography features in the nanometer range. The extracted piezoresponse signal is characterized by an amplitude A_{1w} and phase Φ. The amplitude A_{1w}, in units of length (picometers), depends on the strength of the electromechanical coupling and the phase Φ is determined by the direction of polarization in the sample region beneath the tip. The phase $\Phi = 0^\circ$ (180°) when the sample polarization is parallel (antiparallel) to the AC field with the surface oscillations in phase (out of phase) with the voltage oscillations. To enhance the signal-to-noise ratio for the small PFM signals, the piezoelectric measurements for the monolayer sample were taken in an AFM platform equipped with a dual AC resonance tracking piezoresponse module (MFP-3D, Asylum Research). At the contact resonance frequency, the cantilever oscillation attains its maximum amplitude. The cantilever response amplitude is effectively multiplied by the quality factor (Q) of the cantilever ($Q \sim 10$–100).

In PFM domain imaging, the DC voltage V_{DC} is generally kept at zero value and the cantilever tip subjected to an AC voltage scans the sample material to provide the piezoresponse amplitude and phase images. The images provide information about the location and polarity of the polarization domains in the sample. Figures 3(b), 3(c) and 3(d) represent the sample topography, the amplitude domain, and the phase image, respectively. The PFM topography and the corresponding height profile [Figs. 3(b) and 3(e)] indicate that the measured sample is a triangular-shaped monolayer. The piezoelectric contrast between the TMDCA sample (triangular region) and the SiO_2/Si substrate [Fig. 3(c)] and the piezoresponse profile [Fig. 3(f)] along the indicated line in Fig. 3(c) clarify that the observed piezoelectric response originates from the sample. The piezoresponse may further be analyzed through the plots of the amplitude (strain) A_{1w} versus V_{DC} and the phase Φ versus V_{DC} in the presence of

the AC probing voltage. The DC voltage ranges over both negative and positive values and changes the polarization direction while the AC voltage is needed for the simultaneous measurement of the piezoresponse. The observation of hysteresis in the phase and amplitude plots provides signatures of ferroelectric and piezoelectric behavior, respectively [31]. In ferroelectrics, the polarization arising due to the existence of permanent dipole moments can be switched by an external electric field. The amplitude and phase plots of the monolayer TMDC are shown in Figs. 3(g) and 3(h). In the amplitude plot, the part having the shape of a butterfly (inset) appears in the DC voltage range -1.5 V to $+1.5$ V.

The butterfly shape has its origin in the inverse piezo effect with the strain linearly proportional to the applied electric field giving rise to the linear branches in the butterfly loop. In the case of a polarized domain, the sample expands (contracts) when the electric field and the polarization are aligned parallel (antiparallel). Along the branch pq (inset), for example, the polarization is parallel to the field and the strain increases in magnitude via expansion as the applied voltage increases. The path from q to p, obtained by decreasing the applied voltage, coincides with the path from p to q. When the decreasing DC voltage turns negative, the polarization becomes antiparallel to the electric field and the sample contracts. At the point r, the applied field is sufficiently strong to bring about a change in the polarization direction so that the polarization becomes parallel to the field. Following this train of argument and taking account of the fact that a second switch in the polarization direction occurs at the point t, the butterfly loop is recovered when a full cycle of changes in the DC voltage is executed, as shown by the arrow directions on the branches. A detailed description of the changes along the different branches of the loop in the ideal case is given in [31]. The phase plot provides clear evidence of hysteresis with sharp, approximately 150° changes in polarization direction. The deviation from the ideal phase reversal value of 180° can be attributed to a number of reasons including sample imperfections and the specifics of the experimental measurements. In the vertical PFM mode of the measurements, the polarization is associated with an intrinsic net dipole moment in the vertical direction, the orientation of which (up or down) can be changed by a DC applied field. The twin features of hysteresis in the experimental amplitude and phase plots and the evidence of local polarization switches provide confirmatory evidence of an intrinsic out-of-plane electric dipole moment [7,32–34]. The experimental evidence is in conformity with the first-principles computational results, with the computed intrinsic electric field of the dipole causing a Rashba split at the Γ point (Fig. S4 [14]).

Additionally, the PFM study of the SiO_2/Si substrate (Fig. S9 [14]) does not show any characteristic piezoresponse (e.g., polarization switching), revealing that the piezoelectric behavior solely originates from the TMDCA sample. The piezoelectric coefficient d_{33} is computed from the formula $A_{1w} = d_{33}V_{AC}Q$ as $d_{33} = 1.54 \pm 0.01$ pm/V for $Q = 100$. The value lies in the range of 0.1–2 pm/V reported for polar semiconductors. The value quoted for the Janus MoSSe sample is 0.10 pm/V [7]. It should be noted that the reported d_{33} values are qualitative as the effective piezoelectricity of the samples may be sensitive to small variations in the electrical properties. In this context, it is pertinent to point out that in the case of the randomized MoSSe alloy the experimental evidence is that of a negligible out-of-plane electric dipole moment [7]. To gain further insight, we repeated the same measurements on the bilayer TMDCA (Figs. S10a, S10d [14]). Here, a clear piezoelectric amplitude and phase contrast between the sample and substrate is visible (Figs. S10b, S10c [14]). The line profile depicts a noticeable change in the piezoelectric amplitude for the bilayer compared to the substrate (Fig. S10e [14]). The piezoresponse amplitude-voltage butterfly loop and phase-voltage hysteresis loop are presented in Figs. S10f and S10g [14]. It is noteworthy that with an increasing layer number, the piezoelectric amplitude is enhanced by the strong internal electric filed originating from the parallel electric dipoles of the layers. This observation proves that the measured vertical polarization is an intrinsic material property, not stemming from any topological defects [7,33].

3. Valley polarization and photocurrent

The photoresponse to circularly polarized light is governed by valley-dependent optical selection rules due to which the interband optical transitions at the K and K' valleys are selectively coupled to right circularly polarized (RCP) and left circularly polarized (LCP) light, respectively. This differential absorption of circularly polarized light, termed circular dichroism (CD), results in the selective occupation of a CB valley by photoexcited electrons. Due to strong Coulomb interactions, the photoexcited electron in the CB and the hole in the VB bind each other to form an exciton. In the case of monolayer MoS_2, polarized PL experiments provide evidence for two types of excitons: A and B [13]. The optical transitions for the two types of excitons in the TMDCA material are indicated in Fig. 1(b). These excitons are charge neutral and can further lower their energy by capturing an excess electron or hole to form a negatively or positively charged trion. As detailed below, the valley polarization experiment carried out on the TMDCA sample provides evidence for photogenerated A and B excitons, consistent with the scheme depicted in Fig. 1(b).

The exciton-associated valley polarization, achieved via optical pumping, was initially demonstrated for monolayer MoS_2 using polarization-resolved PL [13]. The exciton has a finite lifetime due to the recombination of the constituent electron and hole. The recombination is accompanied by a characteristic PL which is expected to have the same circular polarization as that of the incident light if the exciton recombination primarily occurs in the same valley in which it is generated. From the experimental data, the degree of valley polarization η can be computed as [1,35]

$$\eta = \frac{\mathrm{PL}(\sigma+) - \mathrm{PL}(\sigma-)}{\mathrm{PL}(\sigma+) + \mathrm{PL}(\sigma-)}, \tag{2}$$

where $\mathrm{PL}(\sigma+)$ and $\mathrm{PL}(\sigma-)$ are the RCP and LCP components of the emitted PL intensity. The polarization degree is an indicator of the effectiveness of the optical selection rules as well as the preservation of the identity of the valley charge carriers before recombination. Figure 1(d) shows the

PL intensity versus emission energy of the TMDCA sample with the incident light being right circularly polarized. The light energy is 1.96 eV near on-resonance with the A exciton. The dominant contribution to the PL intensity, with peak position around 1.8 eV, comes from the PL($\sigma+$) component, and the estimated η value is 42.7%. As the PL spectrum (not polarization resolved) of Fig. S8b shows, the PL intensity is mostly due to the A exciton [14]. The deviation from the ideal value of $\eta = 100\%$ can be understood in terms of the exciton valley depolarization via intervalley electron-hole exchange interaction and phonon-mediated intervalley scattering at room temperature [1]. For the monolayer MoS_2, a wide range of values for η has been reported, from 100% to 32% depending on experimental conditions (for example temperature) and sample preparation [36].

The generation of a photocurrent through optical excitation by circularly polarized light is based on the circular photogalvanic effect (CPGE). Due to spin-valley locking and valley-specific optical selection rules, the photoexcited electrons in the CB are both valley and spin polarized. In the presence of local electric fields, the excitons formed due to interband transitions dissociate into free carriers which are accelerated by a source-drain voltage to generate a spin-polarized photocurrent. Since intervalley scattering requires spin-flip as well as momentum conservation, the generation of a quite robust spin-polarized photocurrent is possible. The detection of spin polarization in TMDC samples has been reported using appropriate device setups, e.g., a lateral spin-valve structure with ferromagnetic contacts [12]. In our experiment, we detect only the charge photocurrent, and the data enable us to obtain a quantitative estimate of the polarization degree of the photocurrent. More generally, different microscopic mechanisms contribute to a photocurrent generated by polarized light with polarization ranging from linear to circular [9–11]. The experimental setup for the generation of a photocurrent in response to polarized light is shown in Fig. 4(a). In this setup, the TMDCA is illuminated with light propagating in the x-z plane at an angle of incidence (θ) with respect to the z direction which is normal to the sample plane. A quarter-wave plate (QWP) is used to change the polarization of the light (linearly polarized) incident on it by rotating the plate to change the angle φ between the fast axis of the QWP and the incident light polarization. The degree of circular polarization of the light falling on the sample is given by $P_{\text{circ}} = \sin 2\varphi$. As φ is changed over a 180° period, the light polarization successively changes with linear polarization at the angles $\varphi = 0°$, 90°, 180° ($P_{\text{circ}} = 0$), RCP ($\sigma+$) at $\varphi = 45°$ ($P_{\text{circ}} = 1$), and LCP ($\sigma-$) at $\varphi = 135°$ ($P_{\text{circ}} = -1$). The generated photocurrent is measured in the y direction. The photocurrent density is, in general, described by the phenomenological equation [9,11,12],

$$j_{PC} = C \sin 2\varphi + L_1 \sin 4\varphi + L_2 \cos 4\varphi + D. \quad (3)$$

The first three terms depend on the light polarization angle φ while the last term is polarization independent. The components arise due to different microscopic mechanisms and are distinguished by their φ dependence. The first term on the right-hand side with coefficient C represents the contribution j_{CPGE} to the photocurrent due to CPGE which utilizes the spin-valley coupling and angular momentum optical selection rules to generate a valley-selective spin-coupled photocurrent. The CPGE-induced current is the dominant contributor to j_{PC} for light energy on-resonance with the excitonic (mainly A) transitions and reverses its direction on reversing the polarization of the light from RCP to LCP. The y component of the CPGE current density is given by [37]

$$j_{\text{CPGE,y}} = i \sum_j \gamma_{yj} (\mathbf{E} \times \mathbf{E}^*)_j,\ i(\mathbf{E} \times \mathbf{E}^*)_j = \hat{e}_j E_0^2 P_{\text{circ}}, \quad (4)$$

where γ is a second-rank pseudotensor, j stands for Cartesian coordinates, $\mathbf{E}$ is the complex electric field of light, E_0 its amplitude, $\hat{e} = \mathbf{q}/q$ is the unit vector in the direction of propagation of light with q being the light wave vector inside the sample, and $P_{\text{circ}} = \sin 2\varphi$ is the helicity of the incident light varying from LCP ($P_{\text{circ}} = -1$) to RCP ($P_{\text{circ}} = +1$) illumination. The polarization-angle-dependent factor of $\sin 2\varphi$ in the phenomenological expression for the CPGE current in Eq. (3) thus arises from P_{circ}. The second term on the right-hand side of Eq. (3) with coefficient L_1 represents a spin-independent contribution j_{LPGE} when the illuminating light is linearly polarized, termed the linear photogalvanic effect (LPGE). The origin of LPGE lies in the dissipative scattering of electrons in the sample. The third term on the right-hand side of Eq. (3) with the coefficient L_2 represents the spin-independent contribution j_{LPDE} due to the linear photon drag effect (LPDE) which arises from the transfer of light momentum to electrons. In this case also, the light falling on the sample is linearly polarized. The fourth term D on the right-hand side of Eq. (3) represents a polarization-independent term. One notes that j_{CPGE} is π periodic whereas j_{LPGE} and j_{LPDE} are $\pi/2$ periodic. The π periodicity of j_{CPGE}, the dominant contributor to the photocurrent, indicates that the photocurrent induced by CPGE reverses its direction when the light polarization changes from positive to negative helicity, i.e., from RCP ($\varphi = 45°$) to LCP ($\varphi = 135°$). This feature is not shown by the other two φ-dependent components.

4. Photocurrent under near-on-resonance illumination

To explore the polarization-dependent photoresponse behavior, we employed linearly polarized light with energies of 1.96 eV (near on-resonance, illumination power = 75 μW) to illuminate the sample while maintaining a constant source-drain voltage $V_{ds} = 1$ V. The photocurrent which mainly arises from the A exciton and A trion exhibited a clear dependence on $\sigma+$ and $\sigma-$ excitation, as depicted in Fig. 4(b) (in the case of $\theta \neq 0°$). Three angles of incidence of the illuminating light, $\theta = 0°$, 45°, and 60°, were chosen for the photocurrent measurements. From the fitting (solid lines) of the experimental data (solid points) using Eq. (3), we obtained the values of coefficients C, L_1, and L_2. Figure 4(c) shows the CPGE current $j_{\text{CPGE}} = C \sin 2\varphi$ versus φ for the three angles of incidence. For the nonzero values of θ, the direction of the photocurrent j_{CPGE} is reversed when the polarization angle φ changes from 45° (RCP) to 135° (LCP) with the magnitude of the current being the largest at these φ values. For normal

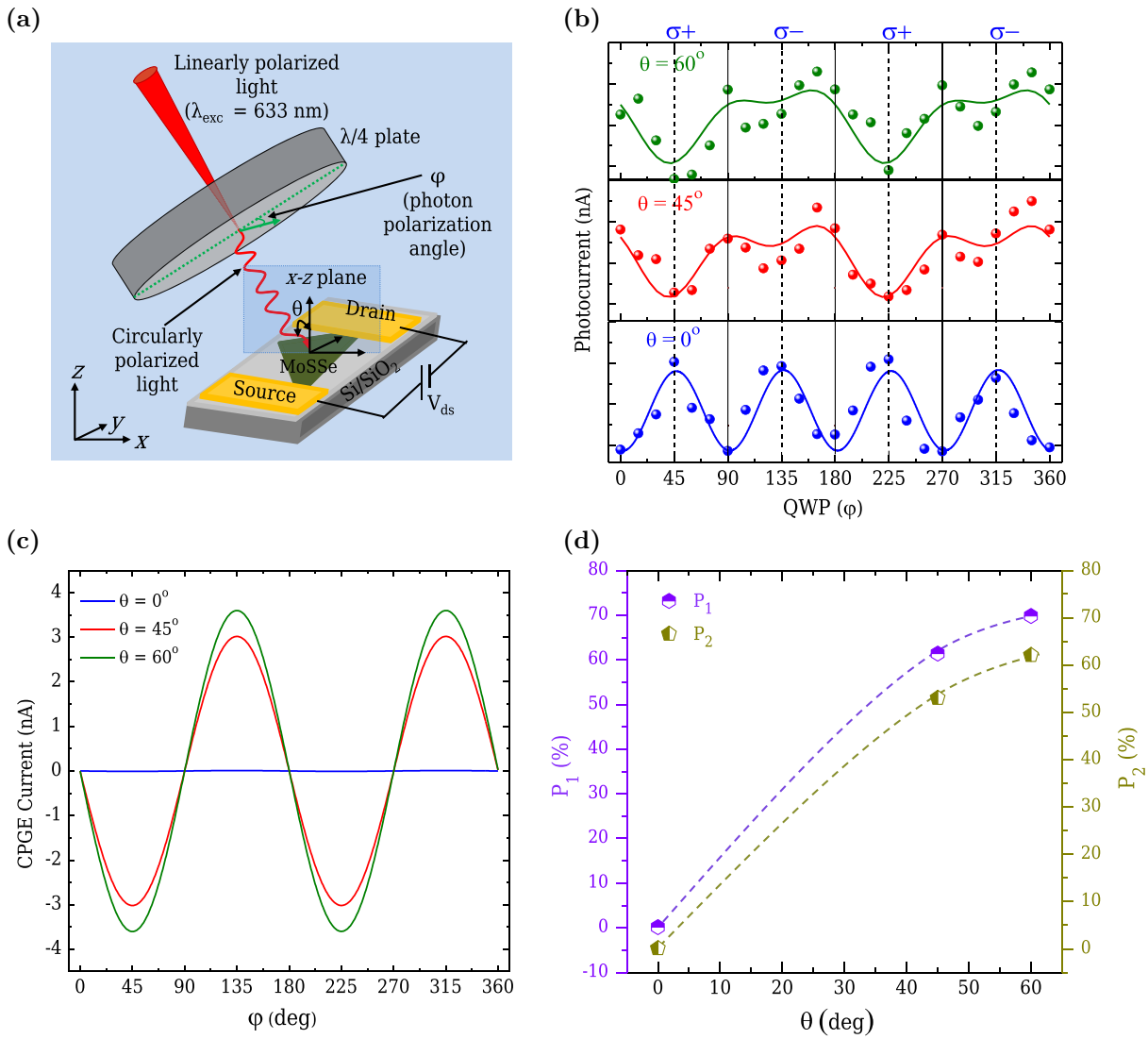

FIG. 4. Experimental configuration, helicity-dependent photocurrent, and degree of polarization at $V_{ds} = 1$ V. (a) Schematic diagram of experimental setup in which the polarization of incoming light is changed by rotating the QWP from 0° to 360°. (b) Photocurrent versus angle of polarization φ using near-on-resonance excitation energy of 1.96 eV (angle of incidence $\theta = 0°$, blue plot; 45°, red plot; and 60°, green plot), with the solid dots representing experimental data. The solid lines are the fitting functions based on Eq. (3). (c) Plot of the CPGE current versus φ. (d) Degree of photocurrent polarization P_1 and P_2 for $\theta = 0°$, 45°, and 60° at 1.96 eV excitation energy.

incidence of light, $\theta = 0°$, the magnitude of the CPGE current turns out to be zero. The maximum amplitude of the CPGE current is attained for $\theta = 60°$. Figure S11a shows the variation of the absolute values of the coefficients C, L_1, and L_2 as a function of θ [14]. One can define a polarization degree of photocurrent P as [37]

$$P = \frac{I(\sigma+) - I(\sigma-)}{I(\sigma+) + I(\sigma-)}, \tag{5}$$

where $I(\sigma+)$ and $I(\sigma-)$ represent the photocurrent generated by RCP and LCP optical excitation, respectively. Using the expression for the photocurrent in Eq. (3), the polarization degree can be negative or greater than 1 since the fitting parameters C, L_1, and L_2 can have positive or negative sign. To keep P positive as well as less than 1, one can use a new definition P_1 of polarization degree as

$$\begin{aligned} P_1 = {} & |[C\sin 2(\sigma+) + L_1 \sin 4(\sigma+) + L_2 \cos 4(\sigma+)] \\ & - [C\sin 2(\sigma-) + L_1 \sin 4(\sigma-) + L_2 \cos 4(\sigma-)]| \\ & \times 1/[|C\sin 2(\sigma+)| + |L_1 \sin 4(\sigma+)| + |L_2 \cos 4(\sigma+)| \\ & + |C\sin 2(\sigma-)| + |L_1 \sin 4(\sigma-)| + |L_2 \cos 4(\sigma-)|], \end{aligned} \tag{6}$$

where $\sigma+$, $\sigma-$ correspond to $\varphi = 45°$, 135°, respectively. The unpolarized contribution D is left out from the calculation. Plugging in the values of φ, one gets

$$P_1 = \frac{|C|}{|C| + |L_2|}. \tag{7}$$

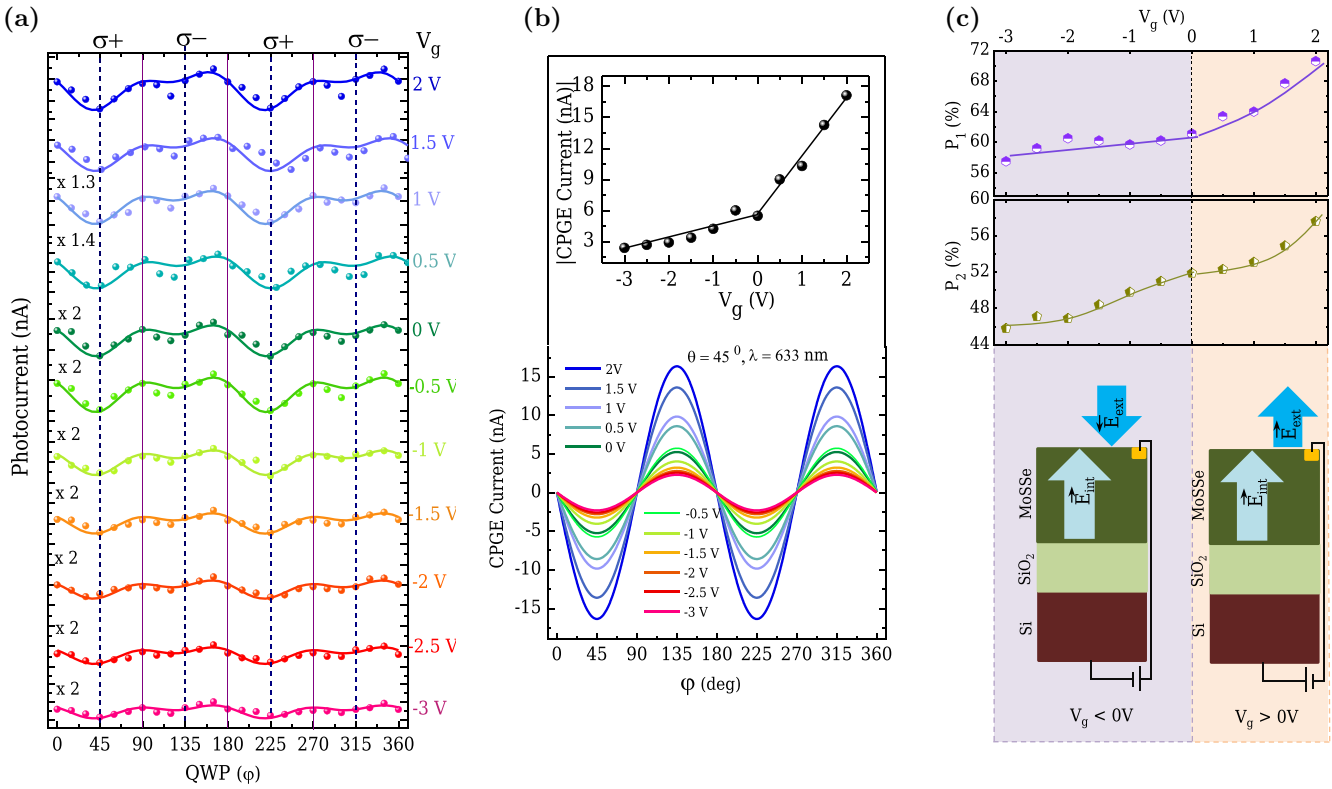

FIG. 5. Gate-voltage-tuned helicity-dependent photocurrent measurement at $V_{ds} = 1$ V. (a) Photocurrent data (solid dots) with gate voltage (V_g) varied from -3 V to $+2$ V under near-on-resonance excitation (1.96 eV) with $\theta = 45^\circ$. The solid lines are the fitting functions. (b) Graphical representation of CPGE current ($C \sin 2\varphi$) as a function of QWP angle φ for all gate voltages with $\theta = 45^\circ$. The solid lines are the fitting functions based on the photocurrent expression in Eq. (3). Inset shows the CPGE current as a function of V_g for $\theta = 45^\circ$. (c) Degrees of photocurrent polarization P_1 and P_2 as functions of gate voltage. Lower panel shows schematically the internal electric field E_{int} and external electric field E_{ext} with the latter arising from gate voltage V_g.

An alternative expression used in the literature [12] is

$$P_2 = \frac{|C|}{|C| + |L_1| + |L_2|}. \tag{8}$$

This is the ratio between the absolute value of the coefficient of j_{CPGE} and the sum of the absolute values of the coefficients of all the polarization-dependent contributions to the total photocurrent. The absolute values of the coefficients represent the maximum values of the corresponding components of the photocurrent. For the data reported in Fig. 4(b), the values of the fitting parameters are $C = -3.77$ nA, $L_1 = -0.67$ nA, $L_2 = 1.63$ nA for $\theta = 60^\circ$. The polarization degrees of the photocurrent are $P_1 = 69.8\%$, $P_2 = 62.1\%$. Figure 4(d) illustrates the variation of P_1 and P_2 values with respect to θ. These results clearly demonstrate the successful generation of a substantial photocurrent polarization, achieved naturally without the need for any external manipulation or intervention. The figure of merit of photocurrent polarization can be defined as [9]

$$F = \frac{|C|}{|L_2|}. \tag{9}$$

The plot of F versus the angle of incidence of illumination light is shown in Fig. S11b [14]. It is observed that F reaches its maximum value for $\theta = 60^\circ$. To check the repeatability of the helicity of light-dependent photocurrent, we have performed the measurements on an additional two monolayer TMDCA based devices and the results are displayed in Fig. S12 [14].

5. *Photocurrent under external electric field*

To explore the effects of an external perpendicular electric field on photocurrent generation under polarized light in monolayer TMDCA, an external gate voltage (V_g) was applied to the sample and varied from -3 V to $+2$ V at a constant drain-source voltage (V_{ds}) of 1 V. Electrostatic gating offers a standard procedure for modulating the photoresponse of TMDC materials [13]. The gate-voltage dependence of the total photocurrent as well as its dominant component, the CPGE current, has been well explored in Refs. [9,10,12,13]. The key results of our study are presented in Fig. 5(a). We utilized a near-on-resonance light source with energy of 1.96 eV (illumination power of 75 μW) and an angle of incidence (θ) of 45°. The specific angle of incidence is chosen to better address experimental challenges. The CPGE current under varying gate voltage is depicted in Fig. 5(b). Figure 5(c) demonstrates the variation of the photocurrent polarization degree P_1 and P_2 with gate voltage. The absolute values of fitted parameters (L_1 and L_2) and F value as a function of gate voltage are displayed in Figs. S13a and S13b, respectively [14]. This study demonstrates the tunability of the photocurrent, the CPGE current,

and the photocurrent polarization degree, by varying the external voltage. As V_g increases beyond 0 V, both the CPGE current and the P_1 or P_2 values are enhanced significantly. Conversely, for $V_g < 0$ V, both the values decrease gradually. The experimental data indicate that a positive gate voltage is aided by the internal electric field E_{int} in increasing the magnitude of a photocurrent as both are aligned in the positive z direction, shown schematically in the lower panel of Fig. 5(c). The oppositely directed negative gate voltage, on the other hand, reduces the effect of the internal field. The computed dipole moment (per unit cell) via first-principles calculations as a function of the external electric field, E_{ext}, is shown in Fig. S4b [14]. We explored the possibility of the contribution of the Rashba effect to the generation of the photocurrent in the TMDCA material. The generation of a CPGE current due to direct interband transitions at the Γ point has been reported in experiments involving quantum well structures [37]. The electronic energy band structures of both monolayer and bilayer TMDCA (Fig. 2 and Fig. S6b [14]) rule out the possibility of direct transitions as the lowest conduction band at the Γ point lies much higher than the CB minimum at the K points. The other possibility lies in an indirect band-gap transition from the VB branches at the Γ point to the CB at the K point [38,39]. PL measurements (Fig. S14 [14]) for excitation energy of 2.54 eV rule out this possibility in the case of a few-layer TMDCA material as the PL intensity spectrum shows that direct transitions are significantly more favorable than indirect ones. In the limit of the bulk material, the direct and the indirect transitions are both favored.

6. Photocurrent under off-resonance illumination

In a subsequent experiment, we replicated the procedure of obtaining polarization-resolved PL spectra using a near-off-resonance excitation of 2.54 eV. The PL spectra are depicted in Fig. S15 [14], exhibiting a valley polarization degree of $\eta = 30.6\%$ [Eq. (2)]. The result is in sharp contrast with that obtained in the case of monolayer MoS_2 using a polarized excitation of 2.33 eV, off-resonance with the A or B exciton [35]. The observed emission was found to be fully unpolarized with $\eta = 0\%$. The degree of polarization of the PL was found to be high when the excitation was on-resonance but had a power-law decrease as the excitation energy increased [36]. Phonon-assisted intervalley scattering has been identified as the primary mechanism for valley depolarization. A finite value of η for the monolayer TMDCA when the excitation is off-resonance signifies that the valley polarization is more robust in the case of the alloy material. A similar feature was observed in the case of the monolayer TMDC material WS_2 using an off-resonance polarized excitation of 2.33 eV, with $\eta = 16\%$ at a temperature of 10 K [40]. The value of $\eta = 30.6\%$ obtained in the case of the alloy material at room temperature signifies a comparatively more robust valley polarization. Unlike in the case of monolayer MoS_2, the depolarization mechanism may not be solely dictated by the off-resonance condition. Figure S16a shows the plot of photocurrent versus the photon polarization angle φ with the angles of incidence $\theta = 60^\circ$, 45°, 0° using an off-resonance excitation of 2.54 eV [14]. For the first two angles of incidence, there is significant polarization between the $\sigma+$ and $\sigma-$ excitations with the degrees of photocurrent polarization given by $P_1 = 52.5\%$ and $P_2 = 36.7\%$. For near-on-resonance excitation of 1.96 eV, $P_1 = 69.8\%$ and $P_2 = 62.1\%$. In comparison, the degree of photocurrent polarization is negligible (less than 1%) in the case of monolayer MoS_2 when the excitation is off-resonance [9]. Figure S16b shows the CPGE current, j_{CPGE}, versus φ for three angles of incidence in the off-resonance condition [14]. The magnitude of the CPGE current, for $\theta = 60^\circ$ and 45°, is non-negligible, in contrast to the case of monolayer MoS_2. It is important to note that the η values obtained from PL measurements, for both near-on-resonance and off-resonance excitations, are smaller compared to the polarization degree of the photocurrent. This can be attributed to the loss of polarization during excitation with circularly polarized light and the subsequent collection in PL measurements [9]. Room-temperature valley polarization under off-resonance excitation in TMDCA offers a new paradigm for valleytronics applications.

7. Photocurrent in bilayer TMDCA

To provide a comparative analysis, we conducted identical measurements on a bilayer TMDCA-based device (the height profile is illustrated in Fig. S17a [14]) without the application of any external electric field. The system was subjected to circularly polarized excitation with an energy of 1.96 eV. The polarization-dependent photocurrent measurement and the values of the fitted parameters are summarized in Figs. S17b and S17c, respectively [14]. The degrees of photocurrent polarization, P_1, P_2, and the F are calculated to be 70.4%, 55%, and 2.38, respectively, with the angle of incidence $\theta = 45^\circ$. To gain a deeper understanding of the underlying mechanisms contributing to the results, we performed DFT calculations for the bilayer TMDCA (Se = 25%, S = 75%). Unlike its parent TMDCs such as MoS_2 and $MoSe_2$, the asymmetric arrangement of S and Se atoms on both sides of the Mo atoms in the bilayer alloy confers on it the character of a noncentrosymmetric crystal and shows an out-of-plane dipole moment as confirmed by PFM study (Fig. S10 [14]). The DFT calculations elucidate the spin-valley physics of the bilayer, akin to the monolayer, revealing a noteworthy splitting of the valence band (VB) with in-plane spin orientations of the band electrons and Rashba splitting around the Γ point, as illustrated in Figs. S6b–S6e [14]. The generation of valley polarization in the bilayer material, even in the absence of an external electric field, considerably enhances its application potential.

IV. DISCUSSION

Our study, involving both experiments and first-principles calculations, establishes that the TMDCA monolayer material $MoS_{2x}Se_{2(1-x)}$ ($x = 0.6$) exhibits the characteristic features of spin-valley physics at the K and K' points and a Rashba splitting of the VB at the Γ point. We have provided a comparison in Table I of the performance of our device vis-à-vis other similar devices reported in literature. As shown in the table, the range of gate voltages required to modulate the photocurrent in the TMDCA material is small, about a few

TABLE I. Comparison of helicity-dependent photocurrent measurements.

Synthesis method	Sample Material	Source-drain bias	Gate voltage	Wavelength of radiation used for Illumination	Illumination power density/power	Angle of incidence	Polarization degree (P) $P_1 = \frac{\lvert C\rvert}{\lvert C\rvert+\lvert L_2\rvert}$	Polarization degree (P) $P_2 = \frac{\lvert C\rvert}{\lvert C\rvert+\lvert L_1\rvert\lvert L_2\rvert}$	Reference
CVD	Monolayer MoS_2	2 V	−40 V	633 nm	100 $mWcm^{-2}$	45°	66%	51.5%	[9]
Mechanical exfoliation	Monolayer $MoSe_2$	1 V	0 V	785 nm	0.8 mW	20°	–	–	[10]
Mechanical exfoliation	Bulk WSe_2	–	0.3 V	1064 nm	<0.5 W	60°	–	–	[11]
Mechanical exfoliation	BulkWSe_2/ graphene/ Bi_2Se_3	0 V	1.5 V	1064 nm	10 μW	30°	67.8%	55%	[12]
Mechanical exfoliation	Monolayer MoS_2	5 V	100 V	650 nm	< 30 μW	45°	∼81%	∼56%	[13]
CVD	Monolayer TMDCA	1 V	0 V	633 nm	75 μW	60°	69.8%	62%	
	Bilayer TMDCA	1 V	0 V	633 nm	75 μW	45°	70.4%	55%	This Work

volts. With a comparatively low laser power density, our photocurrent setup could generate large degrees of photocurrent polarization at room temperature. The significant advantages, already pointed out, call for a wider exploration of TMDCA and related Janus materials as possible device materials in valleytronics applications.

A fundamental quantity which differentiates between the K and K' valleys is the Berry curvature $\mathbf{\Omega}$, interpreted as an effective magnetic field in momentum space [1,2,5]. The Berry curvature is a pseudovector with an out-of-plane orientation and opposite signs at the two valleys. The valley Hall effect, demonstrated experimentally in monolayer MoS_2 [41], has its origin in the opposite signs of the Berry curvature at the two valleys so that the electrons belonging to these valleys move in opposite transverse directions in the presence of an in-plane electric field. An externally applied magnetic field is not needed to observe this Hall-like phenomenon. In the case of gated/polar TMDCs, the electrons at the K, K' valleys experience both Zeeman-type (Ising) and Rashba spin-orbit interactions. For such materials, an intriguing proposal has been made of a novel type of valley Hall effect termed spin-orbit coupling induced spin Hall effect [42] in which a significant enhancement of the spin-type Berry curvature over the orbital Berry curvature at the CB edge, under tunable external gating, could result in a prominent spin-valley Hall effect. A recent theoretical study [26] has shown that the Rashba spin-orbit interactions enhance the spin Hall effect in the monolayer Janus material MoSSe. The experimental demonstration [43,44] of superconductivity, with a highest T_c of 10 K in gated thin films of MoS_2, is another phenomenon the origin of which lies in the coexistence of Ising and Rashba spin-orbit interactions, an intrinsic feature of the Janus and TMDCA materials. The possibility of the contribution of the Berry curvature to a CPGE photocurrent was first discussed in a theoretical study [43]. In this case, the CPGE current j_{CPGE} has a θ dependence of $\cos\theta$ so that the Berry curvature contribution is maximized for $\theta = 0°$, i.e., for normal incidence of the illuminating light [10]. Experiments involving monolayer TMDCs as well as TMDCA rule out a Berry curvature contribution to the CPGE current as the current has finite values only for oblique angles of light incidence, i.e., $\theta \neq 0°$. A recent study [44] provides examples of experimental conditions which allow for the generation of a CPGE current at normal incidence of light. Both the monolayer TMDCA and the monolayer Janus MoSSe possess an intrinsic electric field perpendicular to the monolayer surface. The field contributes to the generation of the Rashba spin-orbit interactions, at the core of applications in spintronics and optoelectronics. The added advantage of the TMDCA is its ease of synthesis making it more suitable for device applications. The TMDCA materials have so far received scant attention from researchers. It is to be hoped that our experimental and computational results on a specific TMDCA material will stimulate further research on polar TMDC materials like Janus and TMDC alloys.

V. CONCLUSION

In summary, we have successfully demonstrated helicity-dependent photocurrent generation in TMDCA material. Notably, a large polarization degree of 62% in monolayer TMDCA is achieved under on-resonance excitation at room temperature, aligning with our helicity-dependent PL study. Even under off-resonance excitation, a small yet discernible valley polarization is observed. First-principles calculations have provided a comprehensive insight into spin-valley coupling, revealing the presence of an inherent out-of-plane electric field. Additionally, PFM measurements have

corroborated the existence of an out-of-plane dipole moment in both mono- and bilayer samples. The polar nature of bilayer TMDCA, along with the breaking of inversion symmetry and spin-valley coupling, offers valuable insights into generating circularly polarized photocurrents with a significant polarization degree. The optical and electrical modulation of photocurrent in TMDCA holds profound implications for fundamental physics and enhanced functionality in the realms of valleytronics and quantum information.

ACKNOWLEDGMENTS

We acknowledge Sanjib Naskar, Indian Association for the Cultivation of Science, for his technical support throughout the PFM study. C.N. acknowledges the INSPIRE Fellowship Programme, Department of Science & Technology, Government of India, for granting her a research fellowship with Registration No. IF180057. S. Masanta expresses gratitude to the Council of Scientific & Industrial Research (CSIR), India, for the financial support provided through the NET-SRF award [File No. 09/015(0531)/2018-EMR-I]. S.G. acknowledges the computational resources provided by the Swedish National Infrastructure for Computing (SNIC) at NSC, PDC, and HPC2N partially funded by the Swedish Research Council (Grant No. 2018-05973). A.N.P. acknowledges DST Nano Mission: DST/NM/TUE/QM-10/2019. I.B. acknowledges the support of NASI, Allahabad, India, under the Honorary Scientist Scheme. A.S. acknowledges financial support from the Science and Engineering Research Board (SERB), India (File No. EMR/2017/002107).

C.N. and A.S. conceived and designed the experiments. C.N. and S. Masanta synthesized the 2D TMDCA and performed the experiments. C.N., S. Masanta, and A.S. analyzed the data. S. Moulick and A.N.P. fabricated the devices and participated in the AFM study. S.G. performed first-principles DFT calculations. I.B. performed the theoretical model calculations and contributed toward conceptualization and physical interpretations. C.N., S.G., I.B., and A.S. contributed to the writing of the manuscript.

[1] J. R. Schaibley, H. Yu, G. Clark, P. Rivera, J. S. Ross, K. L. Seyler, W. Yao, and X. Xu, Valleytronics in 2D materials, Nat. Rev. Mater. **1**, 16055 (2016).

[2] X. Xu, W. Yao, D. Xiao, and T. F. Heinz, Spin and pseudospins in layered transition metal dichalcogenides, Nat. Phys. **10**, 343 (2014).

[3] K. F. Mak and J. Shan, Photonics and optoelectronics of 2D semiconductor transition metal dichalcogenides, Nat. Photon. **10**, 216 (2016).

[4] Y. Liu, Y. Gao, S. Zhang, J. He, J. Yu, and Z. Liu, Valleytronics in transition metal dichalcogenides materials, Nano Res. **12**, 2695 (2019).

[5] D. Xiao, G. B. Liu, W. Feng, X. Xu, and W. Yao, Coupled spin and valley physics in monolayers of MoS_2 and other group-VI dichalcogenides, Phys. Rev. Lett. **108**, 196802 (2012).

[6] L. Du, M. Liao, G. B. Liu, Q. Wang, R. Yang, D. Shi, Y. Yao, and G. Zhang, Strongly distinct electrical response between circular and valley polarization in bilayer transition metal dichalcogenides, Phys. Rev. B **99**, 195415 (2019).

[7] A. Y. Lu, H. Zhu, J. Xiao, C. P. Chuu, Y. Han, M. H. Chiu, C. C. Cheng, C. W. Yang, K. H. Wei, Y. Yang *et al.*, Janus monolayers of transition metal dichalcogenides, Nat. Nanotechnol. **12**, 744 (2017).

[8] L. Zhang, Y. Xia, X. Li, L. Li, X. Fu, J. Cheng, and R. Pan, Janus two-dimensional transition metal dichalcogenides, J. Appl. Phys. **131**, 230902 (2022).

[9] M. Eginligil, B. Cao, Z. Wang, X. Shen, C. Cong, J. Shang, C. Soci, and T. Yu, Dichroic spin-valley photocurrent in monolayer molybdenum disulphide, Nat. Commun. **6**, 7636 (2015).

[10] J. Quereda, T. S. Ghiasi, J. S. You, J. van den Brink, B. J. van Wees, and C. H. van der Wal, Symmetry regimes for circular photocurrents in monolayer $MoSe_2$, Nat. Commun. **9**, 3346 (2018).

[11] H. Yuan, X. Wang, B. Lian, H. Zhang, X. Fang, B. Shen, G. Xu, Y. Xu, S. C. Zhang, H. Y. Hwang *et al.*, Generation and electric control of spin-valley-coupled circular photogalvanic current in WSe_2, Nat. Nanotechnol. **9**, 851 (2014).

[12] S. Cha, M. Noh, J. Kim, J. Son, H. Bae, D. Lee, H. Kim, J. Lee, H. S. Shin, S. Sim *et al.*, Generation, transport and detection of valley-locked spin photocurrent in WSe_2-graphene-Bi_2Se_3 heterostructures, Nat. Nanotechnol. **13**, 910 (2018).

[13] L. Liu, E. J. Lenferink, G. Wei, T. K. Stanev, N. Speiser, and N. P. Stern, Electrical control of circular photogalvanic spin-valley photocurrent in a monolayer semiconductor, ACS Appl. Mater. Interfaces **11**, 3334 (2019).

[14] See Supplemental Material at http://link.aps.org/supplemental/10.1103/PhysRevB.109.115304 for the theoretical derivation and first-principles calculations (Supplemental Note 1); CVD synthesis and details of characterizations of TMDCA (Supplemental Note 2); characterizations of TMDCA device (Supplemental Note 3); piezoelectric force microscopy (PFM) (Supplemental Note 4); $|C|$, $|L_1|$, $|L_2|$, and F values with angle of incidence of illumination under 1.96 eV excitation (Supplemental Note 5); helicity-dependent photocurrent measurements on two additional devices (Supplemental Note 6); $|L_1|$, $|L_2|$, and F values with gate voltage under 1.96 eV excitation (Supplemental Note 7); PL study of few-layer and bulk TMDCA (Supplemental Note 8); helicity-dependent PL study under 2.54 eV excitation energy (Supplemental Note 9); helicity-dependent photocurrent measurements under 2.54 eV excitation (Supplemental Note 10); and helicity-dependent photocurrent measurements of bilayer TMDCA (Supplemental Note 11). It also contains Refs. [15–23].

[15] M. Gmitra, and J. Fabian, Graphene on transition-metal dichalcogenides: A platform for proximity spin-orbit physics and optospintronics, Phys. Rev. B **92**, 155403 (2015).

[16] H. Bentmann, T. Kuzumaki, G. Bihlmayer, S. Blugel, E. V. Chulkov, F. Reinert, and K. Sakamoto, Spin orientation and sign of the Rashba splitting in Bi/Cu(111), Phys. Rev. B **84**, 115426 (2011).

[17] P. Giannozzi, S. Baroni, N. Bonini, M. Calandra, R. Car, C. Cavazzoni, D. Ceresoli, G. L. Chiarotti, M. Cococcioni, I. Dabo *et al.*, Quantum ESPRESSO: A modular and open-source software project for quantum simulations of materials, J. Phys.: Condens. Matter **21**, 395502 (2009).

[18] J. P. Perdew, K. Burke, and M. Ernzerhof, Generalized gradient approximation made simple, Phys. Rev. Lett. **77**, 3865 (1996).

[19] P. E. Blöchl, Projector augmented-wave method, Phys. Rev. B **50**, 17953 (1994).

[20] S. Ghosh, N. Stojić, and N. Binggeli, Rashba-induced spin texture and spin-layer-locking effects in the antiferromagnetic CrI_3 bilayer, J. Phys. Chem. Solids **173**, 111100 (2023).

[21] S. Ghosh, N. Stojić, and N. Binggeli, Structural and magnetic response of CrI_3 monolayer to electric field, Phys. B: Condens. Matter **570**, 166 (2019).

[22] G. Bihlmayer, P. Noël, D. V. Vyalikh, E. V. Chulkov, and A. Manchon, Rashba-like physics in condensed matter, Nat. Rev. Phys. **4**, 642 (2022).

[23] J. Chen, K. Wu, W. Hu, and J. Yang, Spin-orbit coupling in 2D semiconductors: A theoretical perspective, J. Phys. Chem. Lett. **12**, 12256 (2021).

[24] Z. Wang, 2H $\rightarrow$ 1T′ phase transformation in Janus monolayer MoSSe and MoSTe: An efficient hole injection contact for 2H-MoS_2, J. Mater. Chem. C **6**, 13000 (2018).

[25] X. Yang, D. Singh, Z. Xu, Z. Wang, and R. Ahuja, An emerging Janus MoSeTe material for potential applications in optoelectronic devices, J. Mater. Chem. C **7**, 12312 (2019).

[26] S. B. Yu, M. Zhou, D. Zhang, and K. Chang, Spin Hall effect in the monolayer Janus compound MoSSe enhanced by Rashba spin-orbit coupling, Phys. Rev. B **104**, 075435 (2021).

[27] T. Hu, F. Jia, G. Zhao, J. Wu, A. Stroppa, and W. Ren, Intrinsic and anisotropic Rashba spin splitting in Janus transition-metal dichalcogenide monolayers, Phys. Rev. B **97**, 235404 (2018).

[28] A. Bera, A. Singh, Y. A. Sorb, R. N. Jenjeti, D. V. S. Muthu, S. Sampath, C. Narayana, U. V. Waghmare, and A. K. Sood, Chemical ordering and pressure-induced isostructural and electronic transitions in MoSSe crystal, Phys. Rev. B **102**, 014103 (2020).

[29] S. Masanta, C. Nayak, P. Agarwal, K. Das, and A. Singha, Monolayer graphene-MoSSe van der Waals heterostructure for highly responsive gate-tunable near-infrared-sensitive broadband fast photodetector, ACS Appl. Mater. Interfaces **15**, 14523 (2023).

[30] S. Mukherjee, D. Bhattacharya, S. K. Ray, and A. N. Pal, High-performance broad-band photodetection based on graphene-$MoS_{2x}Se_{2(1-x)}$ alloy engineered phototransistors, ACS Appl. Mater. Interfaces **14**, 34875 (2022).

[31] D. Damjanovic, Ferroelectric, dielectric and piezoelectric properties of ferroelectric thin films and ceramics, Rep. Prog. Phys. **61**, 1267 (1998).

[32] S. Xie, A. Gannepalli, Q. N. Chen, Y. Liu, Y. Zhou, R. Proksch, and J. Li, High resolution quantitative piezoresponse force microscopy of $BiFeO_3$ nanofibers with dramatically enhanced sensitivity, Nanoscale **4**, 408 (2012).

[33] F. Xue, J. Zhang, W. Hu, W. T. Hsu, A. Han, S. F. Leung, J. K. Huang, Y. Wan, S. Liu, J. Zhang *et al.*, Multidirection piezoelectricity in mono- and multilayered hexagonal α-In_2Se_3, ACS Nano **12**, 4976 (2018).

[34] G. Rao, H. Fang, T. Zhou, C. Zhao, N. Shang, J. Huang, Y. Liu, X. Du, P. Li, X. Jian *et al.*, Robust piezoelectricity with spontaneous polarization in monolayer tellurene and multilayer tellurium film at room temperature for reliable memory, Adv. Mater. **34**, 2204697 (2022).

[35] K. F. Mak, K. He, J. Shan, and T. F. Heinz, Control of valley polarization in monolayer MoS_2 by optical helicity, Nat. Nanotechnol. **7**, 494 (2012).

[36] G. Kioseoglou, A. T. Hanbicki, M. Currie, A. L. Friedman, D. Gunlycke, and B. T. Jonker, Valley polarization and intervalley scattering in monolayer MoS_2, Appl. Phys. Lett. **101**, 221907 (2012).

[37] S. D. Ganichev and W. Prettl, Spin photocurrents in quantum wells, J. Phys.: Condens. Matter **15**, R935 (2003).

[38] S. Patel, U. Dey, N. P. Adhikari, and A. Taraphder, Electric field and strain-induced band-gap engineering and manipulation of the Rashba spin splitting in Janus van der Waals heterostructures, Phys. Rev. B **106**, 035125 (2022).

[39] L. Du, Q. Zhang, T. Zhang, Z. Jia, J. Liang, G.–B. Liu, R. Yang, D. Shi, J. Xiang, K. Liu, Z. Sun, Y. Yao, Q. Zhang, and G. Zhang, Robust circular polarization of indirect Q-K transitions in bilayer 3*R*-WS_2, Phys. Rev. B **100**, 161404(R) (2019).

[40] B. Zhu, H. Zeng, J. Dai, Z. Gong, and X. Cui, Anomalously robust valley polarization and valley coherence in bilayer WS_2, Proc. Natl. Acad. Sci. USA **111**, 11606 (2014).

[41] K. F. Mak, K. L. McGill, J. Park, and P. L. McEuen, The valley Hall effect in MoS_2 transistors, Science **344**, 1489 (2014).

[42] B. T. Zhou, K. Taguchi, Y. Kawaguchi, Y. Tanaka, and K. T. Law, Spin-orbit coupling induced valley Hall effects in transition-metal dichalcogenides, Commun. Phys. **2**, 26 (2019).

[43] J. E. Moore and J. Orenstein, Confinement-induced Berry phase and helicity-dependent photocurrents, Phys. Rev. Lett. **105**, 026805 (2010).

[44] J. Quereda, J. Hidding, T. S. Ghiasi, B. J. van Wees, C. H. van der Wal, and M. H. D. Guimarães, The role of device asymmetries and Schottky barriers on the helicity-dependent photoresponse of 2D phototransistors, npj 2D Mater. Appl. **5**, 13 (2021).